

RESEARCH ARTICLE

Grain boundary segregation in multicrystalline silicon: correlative characterization by EBSD, EBIC, and atom probe tomography

Andreas Stoffers^{1*}, Oana Cojocaru-Mirédin¹, Winfried Seifert^{2,3}, Stefan Zaefferer¹,
Stephan Riepe⁴ and Dierk Raabe¹

¹ Max-Planck-Institut für Eisenforschung GmbH, Max-Planck-Straße 1, Düsseldorf, 40237, Germany

² Brandenburgische Technische Universität Cottbus, Joint Lab IHP/BTU, Platz der Deutschen Einheit 1, Cottbus, 03046, Germany

³ IHP, Im Technologiepark 25, Frankfurt (Oder), 15236, Germany

⁴ Fraunhofer-Institut für Solare Energiesysteme, Heidenhofstraße 2, Freiburg, 79110, Germany

ABSTRACT

This study aims to better understand the influence of crystallographic structure and impurity decoration on the recombination activity at grain boundaries in multicrystalline silicon. A sample of the upper part of a multicrystalline silicon ingot with intentional addition of iron and copper has been investigated. Correlative electron-beam-induced current, electron backscatter diffraction, and atom probe tomography data for different types of grain boundaries are presented. For a symmetric coherent $\Sigma 3$ twin boundary, with very low recombination activity, no impurities are detected. In case of a non-coherent (random) high-angle grain boundary and higher order twins with pronounced recombination activity, carbon and oxygen impurities are observed to decorate the interface. Copper contamination is detected for the boundary with the highest recombination activity in this study, a random high-angle grain boundary located in the vicinity of a triple junction. The 3D atom probe tomography study presented here is the first direct atomic scale identification and quantification of impurities decorating grain boundaries in multicrystalline silicon. The observed deviations in chemical decoration and induced current could be directly linked with different crystallographic structures of silicon grain boundaries. Hence, the current work establishes a direct correlation between grain boundary structure, atomic scale segregation information, and electrical activity. It can help to identify interface–property relationships for silicon interfaces that enable grain boundary engineering in multicrystalline silicon. Copyright © 2015 John Wiley & Sons, Ltd.

KEYWORDS

multicrystalline silicon solar cells; grain boundaries; atom probe tomography; electron backscatter diffraction; electron beam induced current

*Correspondence

Andreas Stoffers, Max-Planck-Institut für Eisenforschung GmbH, Max-Planck-Straße 1, 40237 Düsseldorf, Germany.

E-mail: a.stoffers@mpie.de

Received 3 December 2014; Revised 25 February 2015; Accepted 10 March 2015

1. INTRODUCTION

Multicrystalline silicon (mc-Si) is a commonly used cost-effective bulk material for solar cell applications [1]. Up to date, the record efficiency registered for mc-Si solar cells is 20.8%, while the one registered for monocrystalline Si solar cells is 25.6% [2]. Contrary to monocrystalline Si, mc-Si contains high densities of defects, such as dislocations, grain boundaries (GBs), and stacking faults, reducing the solar cell efficiency [1]. The model developed by Kveder *et al.* [3] explains how the recombination rate of

the minority charge carriers increases when dislocations are contaminated by transition metal impurities. Because of advanced crystallization techniques, the density of dislocation clusters in mc-Si has been significantly reduced such that the recombination at GBs comes into focus again [4]. For recombination at GBs, no equivalent model for the effects of the impurities on the GBs recombination rates exists [5]. This may be due to generally complex crystallographic structure of GBs, characterized by its misorientation and plane inclination [6]. It has been suggested though that the presence of transition metal impurities at

Si GBs may create deep levels, which induce a higher recombination activity. The main effect is a decrease of the average minority carrier lifetime, which is directly linked with the solar cell efficiency [7].

C and O are well-known impurity species in mc-Si, inherited from the crystallization furnace and the crucible [8]. According to the Gibbs adsorption isotherm, such impurities will segregate to defects, particularly to GBs [9,10]. Only few studies exist though on the impact of these light GB impurities on the recombination activity [11], whereas vast literature exists on the detrimental effects of transition metals, such as Fe, Cr, Ni, and Cu, on the carrier recombination and cell efficiency [12–16]. The critical bulk concentration has been reported to be in the range of 10^{14} at/cm³ for Fe and Cu [13]. Electron-beam-induced current (EBIC) studies suggest that the recombination activity is different from one GB to another [17,18]. Even more remarkable is the fact that the EBIC contrast can change along the same GB [17,19,20]. During the last years, it has been shown that transition metal impurities and light elements segregate mainly at the GBs in the form of heterogeneous precipitates as silicides (such as FeSi₂ [21], NiSi₂ [22], and Cu₃Si [13]), carbides (SiC), and oxides (SiO₂). The presence of these precipitates induces supplementary strong dot-like dark features in EBIC maps mainly at the GBs but cannot alone explain the complexity of the EBIC maps such as recombination-free segments and contrast variations observed along some of the GBs [17].

These early observations clearly show that a complex relationship exists between the crystallographic character of GBs, the type of impurity element segregated to them, and their recombination rates. For this reason, we conducted a systematic analysis of GBs using correlative electron backscatter diffraction (EBSD)–EBIC–atom probe tomography (APT) measurements. The precise correlation requires a challenging site-specific sample preparation. A special sample holder system was developed, which enables us to mount the samples in all the involved microscopes (scanning electron microscope (SEM), focused ion beam (FIB), transmission electron microscope (TEM), EBSD, EBIC, and APT) without changing the retainer and thus facilitates the sample preparation [23,24]. Therefore, a better understanding of corresponding structure-property relationships in mc-Si solar cells is expected, by coupling the local chemistry with the GB type and electrical activity. Moreover, the present 3D APT study is the first correlative EBSD–EBIC–APT study and one of the first direct identification and quantification experiments of impurities decorating GBs in mc-Si [25,26].

2. MATERIALS AND METHODS

In order to make the effects associated with GB impurity segregation clearly visible, the study was conducted on intentionally contaminated p-type Si. The samples were taken from the capping area of an ingot grown in a quartz

crucible coated with industrial quality Si₃N₄ lining, where 20 ppma Fe and 20 ppma Cu were added to the B-doped feedstock during melting of feedstock. Directional solidification was used with a solidification velocity of 1.0–1.1 cm/h. The blocks produced with a small casting furnace have a base area of 270 × 177 mm² and a height of 200 mm. Wafers and solar cells were made by industrial-type processes.

Some features of this ingot were already studied in [27,28], where the properties of different intentionally contaminated samples were compared with an uncontaminated reference sample. Indeed, Figure 1(a) shows the impact of the intentional contamination on the solar cell efficiency. A significant reduction of cell efficiency is observed throughout the whole ingot but especially in the top part. The concentration profiles of different impurity species could be measured with respect to the height of the ingot, as shown in Figure 1(b). Here, Fe and Cu concentration profiles were determined by neutron activation analysis, whereas the concentration profiles of interstitial oxygen O_i and substitutional carbon C_s were determined by Fourier transformed infrared spectroscopy. For the latter only, the concentrations in

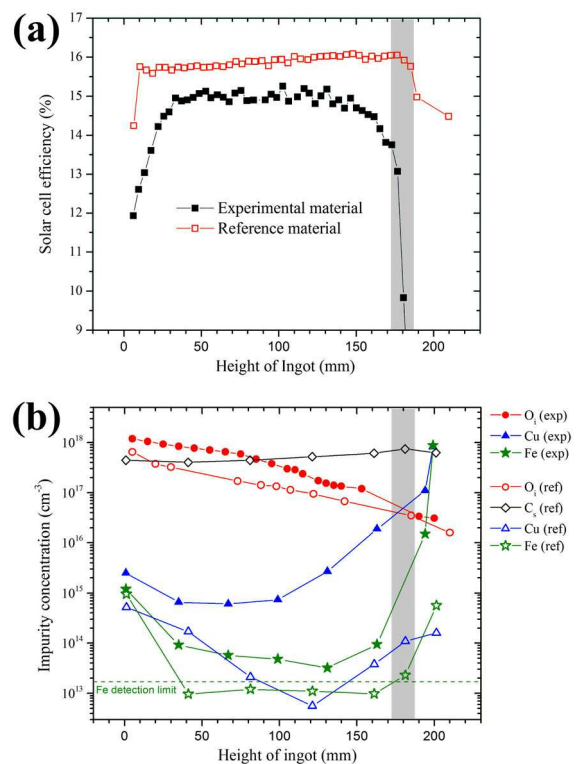


Figure 1. (a) Height-dependent solar cell efficiencies of reference and experimental materials (20 ppma Fe and Cu added). (b) Height-dependent impurity concentration profiles of reference ingot and experimental ingot, measured by neutron activation analysis (Fe and Cu) and Fourier transform infrared (O_i and C_s) [25].

the uncontaminated reference sample were measured, knowing that no substantial difference in C_s concentration is expected in the studied sample (for more details, see [27]). The samples discussed in the present study were taken from a 210- μm -thick wafer from a height of 180 mm (90% of ingot height), where a sharp drop in solar cell efficiency was observed. More precisely, addition of the impurities lowered the efficiency by 1.8%. It is well known that ingots grown by directional solidification contain the highest amount of impurities in the top portion, and thus, we expect also the GB segregation to be most pronounced in this region. We point out that all the correlative studies in the present study were conducted on samples that were taken before the application of any gettering processes or an anti-reflection coating.

The electrical properties of the samples were characterized by conducting EBIC at room temperature. These experiments were performed on a Zeiss EVO 40 SEM equipped with a commercial Gatan EBIC system. A thin Al layer deposited by thermal evaporation served as charge-collecting contact for EBIC. APT experiments were carried out on a local electrode atom probe [29,30] (LEAPTM 3000X HR, Cameca Instruments) applying 12 ps laser pulses with energy of 0.35 nJ at a repetition rate of 160 kHz and a wavelength of 532 nm [31]. A base temperature of 60 K was used. Laser-assisted APT already provided an inside into the chemistry in Cu(In,Ga)Se₂ thin-film solar cells, where impurities also play an important role for the efficiency [32–34]. Sample preparation by Ga-ion milling was performed on a dual beam FIB (FEI Helios Nanolab 600). The same instrument was employed for EBSD analysis (0.8 μm step size) using a Hikari S/N 1040 camera provided by TSL/EDAX. The EBSD scans were performed before deposition of the charge collecting contact. Tips for APT analysis having the GB of interest within the analysis region were manufactured by site-specific preparation method described by Felfer *et al.* [35]. One of the advantages of this advanced preparation method is that the interface of interest lies perpendicular to the tip axis, which minimizes artifacts by the local magnification effect, and its position in the tip can be easily controlled. Electropolished Mo-TEM grids were used as support structure. A self-designed adapter for correlative microscopy enables us to mount these grids easily in all different microscopes involved (EBSD, FIB, TEM, and APT) [24]. Final ion beam milling was performed at 2 kV in order to minimize the damage caused by the Ga ions. TEM analysis of the final APT tips was performed with a JEOL 2200 FS TEM operated at 200 kV in order to resolve the microstructure and determine the position of the GB within the APT tips. Furthermore, TEM experiments using the same instrument were performed to study the presence of defects like steps or dislocations at the GBs. For this work, a thin lamella containing a triple point was prepared as plan view FIB liftout with a final ion milling step at 2 kV.

3. RESULTS

Grain boundaries are characterized by five rotational parameters, namely, the crystallographic misorientation across the boundary (three parameters) and the GB normal vector (two parameters) [36]. All five parameters may influence the chemical and electronic characters of a boundary. The misorientation of a GB is most conveniently expressed by a rotation, defined by the crystallographic axis and rotation angle that transfers the lattice of the first grain into the lattice of the second grain. For random high-angle GBs, it is frequently sufficient to report only the rotation angle. For special boundaries, in particular for twin boundaries (TBs), the misorientation may also be described by its coincidence site lattice (CSL) type expressed by its Σ value. A $\Sigma 3$ value indicates a lattice in first-order twin relationship in cubic materials, for example. Although the CSL concept is sometimes taken as a measure that characterizes the degree of plane matching, it should be noted that the Σ value only describes the misorientation of two lattices; it does not describe, however, the position of the boundary normal vector. This means that for the same CSL value, an interface may reveal different crystallographic matches at atomic scale, depending on its local plane normal. If this normal vector corresponds to the mirror plane of the twin (in face-centered cubic and related lattices, this is the (111) plane for a $\Sigma 3$ TB), the TB is a coherent TB. In all other cases, the boundary is incoherent. When an existing $\Sigma 3$ twin twins again (second-order twin), a $\Sigma 9$ boundary is formed with respect to the original parent crystal, if it twins once again a $\Sigma 27$ TB is formed. These boundaries may be addressed as “higher order” TBs, although their mirror planes are not simple low-indexed boundaries (e.g., (122) or (114) for a symmetric $\Sigma 9$ tilt boundary and (127) for a symmetric $\Sigma 27$ tilt boundary). In the following, we will address the GB type by the following notations: coherent TBs will be indicated by their Σ value together with the coherency plane, incoherent ones only by their Σ value, and random GBs (R) will be defined by the misorientation angle only.

It should be noted that coherent TBs may show two sorts of deviation from their perfect crystallography. The first one is a deviation from their ideal misorientation. Such a deviation is in general accommodated by secondary GB dislocations. The second one is the deviation from their ideal boundary position that is accommodated by small atomic interface steps, which are, as a rule, incoherent zones.

Figure 2 shows an SEM map of a sample area studied in this work together with the most relevant EBSD information and the associated EBIC map. In Figure 2(a), GB character and the angular deviation from the average grain orientation for every grain (from 0° to 1.8°) are shown. Notable at this point is the significant orientation deviation in the right-hand side grain of the SEM map, especially in the vicinity of the triple point. This may be an indicator for imperfect twinning resulting in the formation of dislocations for strain accommodation or/and steps at the GBs.

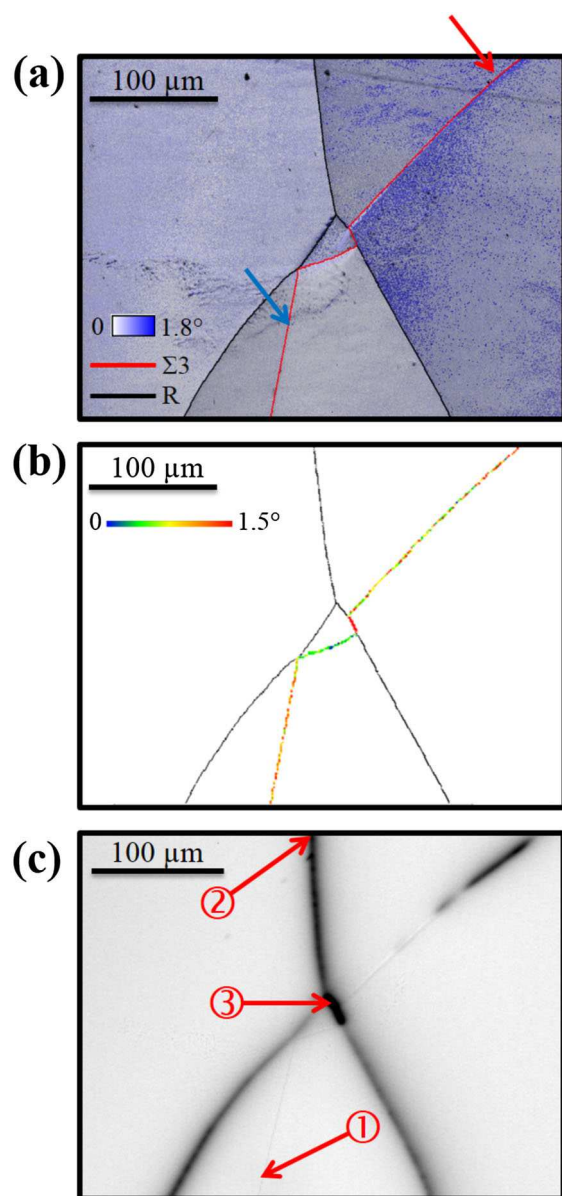


Figure 2. (a) Scanning electron microscope image of studied sample area overlaid with electron backscatter diffraction information on grain boundary crystallography. The deviation in orientation from 0° to 1.8° inside the grains is plotted in this map. (b) Grain boundary map indicating the deviation from ideal $\Sigma 3$ definition. (c) Electron-beam-induced current map of the studied sample area. The red arrows indicate the three positions chosen for detailed atom probe tomography analysis. This figure is available in colour online at wileyonlinelibrary.com/journal/pip.

Ganapati *et al.* [37] and Sarau *et al.* [38] suggested that dislocations are formed in mc-Si in order to relieve thermally induced residual stresses during crystal growth, especially at triple points where the thermal stresses are known to be quite high.

The blue arrow in Figure 2(a) indicates a coherent TB with very small fluctuations in misorientation (0.1° in

average, i.e., within the tolerances of EBSD measurements) and only small deviation from the ideal $\Sigma 3$ misorientation (1.3°). The deviation regime falls well into the Brandon criterion [39]. For obtaining a deeper understanding of the $\Sigma 3$ boundary properties, Figure 2(b) shows the angular deviation in misorientation of the investigated $\Sigma 3$ TBs from the exact $\Sigma 3$ boundary misorientation. Additionally to the misorientation deviation, it is important to assess the deviation of the boundary plane from the ideal (111) boundary position. In the stereographic projection of the (111) planes in Figure 3(b), the locus of all possible boundary normal vectors of the investigated $\Sigma 3$ TB is represented by the red line, which is perpendicular to the boundary trace line in Figure 3(a). The trajectory of possible normal vectors passes exactly through the common (111) poles of the two abutting grains (Figure 3(b)). This position therefore corresponds most likely to the correct boundary normal and indicates that the here investigated boundary is a coherent $\Sigma 3$ (111) TB. The same analysis was carried out for the adjacent $\Sigma 3$ (111) TB, showing also coherent character.

However, not all $\Sigma 3$ TBs shown in Figure 2(a) are coherent. For example, another $\Sigma 3$ TB, marked by a red arrow in Figure 2(a), shows a different character. This boundary is slightly bent, which indicates a transition between two different boundary plane segments marked by orange and blue lines in Figure 3(a). At this particular $\Sigma 3$ TB, the angular deviation from the ideal $\Sigma 3$ misorientation (60° about [111]; i.e., the angular distance between two misorientation matrices) is small: for the lower part (marked in orange in Figure 3(a)), the deviation is in the order of $1.0^\circ \pm 0.4^\circ$, and for the upper part (marked in blue in Figure 3(a)), it is in the order of $1.2^\circ \pm 0.4^\circ$ (each value measured across the boundary at about 15 positions). Note that also the obviously perfect twin marked ① in Figure 2(c) results in a deviation of $1.1^\circ \pm 0.3^\circ$. The aforementioned reported values are thus at the edge of accuracy of the used EBSD measurements and can only be used to report a trend but do not indicate absolute values [40].

More important than the slight deviation from the $\Sigma 3$ misorientation is the difference in boundary plane. The same trace analysis as the one presented earlier shows that the GB is actually not a (111) coherent TB but, most probably, a (112) symmetric incoherent TB (SITB). Such boundaries are characterized by a sharp twin relationship and a common (112) boundary plane on each side of the grains. This common (112) plane is also the mirror plane of the two lattices. The part of the boundary marked in orange in Figure 3(a) is, most likely almost an exact SITB with a deviation between the boundary plane and the common (112) plane being less than $1\text{--}2^\circ$. One has to consider though that the trace analysis cannot make a definite statement on the GB plane but may only suggest a possible one. The part marked in blue, in contrast, deviates by about 10° from the SITB position. According to Wolf *et al.* [41], a deviation of the SITB from the perfectly symmetric position is quite common and can directly be related to the relatively high energy of the SITB.

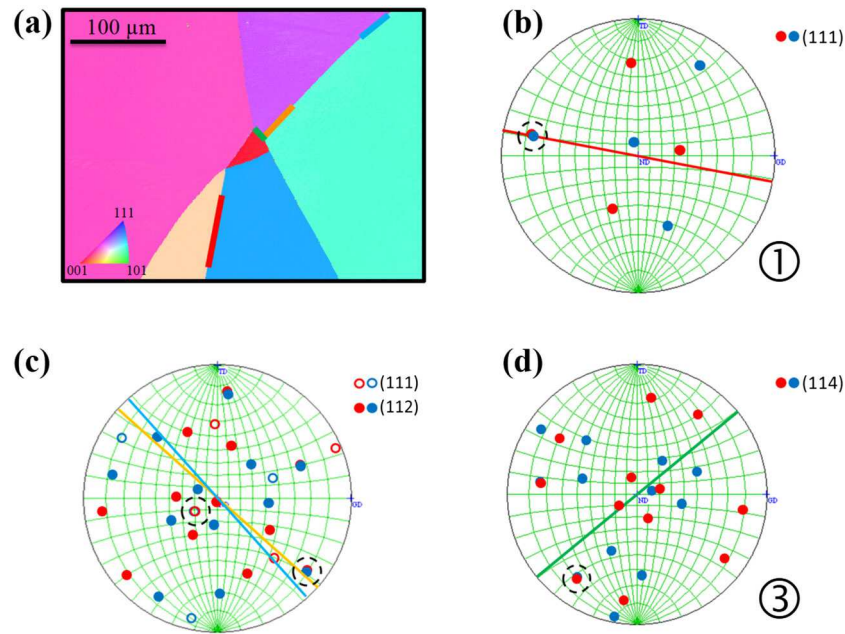


Figure 3. (a) Inverse pole figure map of studied sample area with colored plane traces and the corresponding pole figures for (b) $\Sigma 3$ (111) (red), (c) incoherent $\Sigma 3$ (orange and blue), and (d) incoherent R 32.1° (green). Colored lines in the pole figures represent all possible grain boundary normal vectors of the boundary. This figure is available in colour online at wileyonlinelibrary.com/journal/pip

Position ② in Figure 2(c) is a random GB with a misorientation of $55.4^\circ \pm 0.1^\circ$ and Position ③ is close to a triple point, where the lower part most likely consists of an incoherent $\Sigma 3$ TB with very strong deviation from the exact CSL $\Sigma 3$ definition. Following the “sigma combination rule” [42], the lower part of the GB would be expected to be an incoherent $\Sigma 9$ TB (green line in Figure 3(a) and (d)). However, the measured misorientation angle ($32.1^\circ \pm 0.1^\circ$) has a large deviation from the ideal $\Sigma 9$ misorientation (38.94°), larger than the Brandon criterion, which is 5° for $\Sigma 9$ [39]. The pole figure analysis for this specific GB reveals that it is most probably an asymmetric random boundary plane (R 32.1°). We plot here only the (114) pole figure for demonstration (Figure 3(d)). In this case, the boundary plane is more than 10° off.

An accurate investigation of the GB crystallography as conducted earlier is essential for understanding the electrical behavior of GBs, because it can already give an indication for possible structural defects, as shown also by Chen *et al.* [43] for different $\Sigma 3$ TBs. Indeed, the properties of coherent and incoherent TBs in general can be profoundly different. More specific, coherent TBs are immobile during grain growth and have practically no free volume compared with the surrounding lattice. In contrast, incoherent TBs can accommodate impurities more easily and can also be very mobile [44]. Also, incoherency can be accommodated by surface steps and GB dislocations. We must recall in this context that the signal recorded with the EBSD method used here results from an interaction volume of at least $100 \times 50 \times 20 \text{ nm}^3$. This volume may be large with respect to surface steps on TBs, which can have atomic

dimensions. This is why a GB, which appears as a straight line in the EBSD map, may actually contain steps at the nanoscale, that is, a GB that appears to be fully incoherent in EBSD can contain small coherent and incoherent portions at near-atomic scale. Straight coherent boundaries, in contrast, are accurately described by EBSD. Because the incoherent TB portion is often realized by a group of partial dislocations or surface steps, these areas have higher free volume and thus substantial elastic distortion fields around them are expected. Sarau *et al.* [38] have recently found that the internal stresses around dislocations are generally too small (several tens of megapascal) and do not directly influence their electrical activity. However, because of these internal stresses, the accumulation of impurities at such dislocations is promoted in order to locally relax the strain energy. Thus, being decorated by impurities, the dislocations or GBs can become electrically active and show minority carrier recombination.

The EBIC map in Figure 2(c) gives an overview of the recombination activity in the area shown in Figure 2(a). There is a strong variation of the EBIC contrast from one GB to another (see contrast values in Table I). The contrast C is defined by $C = \frac{I_0 - I_{GB}}{I_0}$, where I_{GB} and I_0 are the measured currents at the GB and in the defect-free region far away from it. The EBIC contrast values provide direct information on the recombination activity of the GBs.

We observed low recombination activity for $\Sigma 3$ (111) coherent TBs, whereas moderate and very high recombination activity was detected for incoherent TBs and random GBs. For example, the measured recombination contrast at Position ① is negligible ($<1\%$). Indeed, the very weak

Table I. Electron-beam-induced current contrast and Gibbs' interfacial excess values.

| GB | ID | Misorientation (°) | EBIC contrast (%) | Γ_C (at/nm ²) | Γ_O (at/nm ²) | Γ_{Cu} (at/nm ²) | Γ_{total} (at/nm ²) |
|------------------|----|--------------------|-------------------|----------------------------------|----------------------------------|-------------------------------------|----------------------------------------|
| $\Sigma 3$ (111) | ① | 59.9 ± 0.1 | <1 | — | — | — | — |
| $\Sigma 3$ (111) | ① | 59.9 ± 0.1 | <1 | — | — | — | — |
| $\Sigma 3$ (111) | | 59.7 ± 0.1 | <1 | — | — | — | — |
| $\Sigma 9$ | | 38.4 ± 0.1 | >>1* | 0.13 ± 0.01 | — | — | 0.13 ± 0.01 |
| $\Sigma 9$ | | 38.4 ± 0.1 | >>1* | 0.15 ± 0.01 | — | — | 0.15 ± 0.01 |
| $\Sigma 9$ | | 38.4 ± 0.1 | >>1* | 0.23 ± 0.01 | — | — | 0.23 ± 0.01 |
| $\Sigma 27b$ | | 35.0 ± 0.1 | 29 ± 1 | 0.15 ± 0.01 | 0.17 ± 0.01 | — | 0.32 ± 0.02 |
| R | ③ | 32.1 ± 0.1 | 53 ± 1 | 0.15 ± 0.01 | — | 0.12 ± 0.01 | 0.27 ± 0.02 |
| R | ② | 55.4 ± 0.1 | 25 ± 1 | 0.21 ± 0.01 | 0.19 ± 0.01 | — | 0.40 ± 0.02 |

EBIC, electron-beam-induced current; GB, grain boundary.

*Only qualitative EBIC data available.

contrast observed for Position ① is not caused by carrier recombination but because of the topography change at the GB. The incoherent $\Sigma 3$ (112) TB indicated by a red arrow in Figure 2(a) shows a recombination-free segment at the lower part and elevated recombination activity at the upper part, where the boundary plane position strongly deviates from the ideal twin relation. The difference in boundary plane deviation can be an explanation for the different EBIC behaviors of these two GB regions. At Position ②, the EBIC contrast is $25\% \pm 1\%$ (Table I). The misorientation across this random GB is 55.4° . The highest EBIC contrast was measured in the vicinity of Position ③, namely, $40\% \pm 1\%$ for the strongly deviating $\Sigma 3$ TB located below the triple point and $53\% \pm 1\%$ for the random GB above the triple point. Again, these high recombination activities can be attributed to the high degree of incoherency of these boundaries.

The red arrows in Figure 2(c) indicate the exact positions (①, ②, and ③) chosen for further APT analysis. Figure 4(a) shows a TEM image of the final APT tip taken from Position ① with the corresponding 3D elemental map (Figure 4(b)). The TEM image clearly resolves the GB position at 67 nm away from the apex of the tip. This kind of correlative FIB–TEM sample preparation was carried out for every single APT tip. The procedure is crucial not only for identifying the precise location of the GB within the tip but also for improving the accuracy of the 3D reconstruction of the APT data: radius, shank angle, and other structural information that can be directly taken into account, when conducting the atom probe reconstruction [45–47]. The APT analysis was performed up to a depth of 180 nm, revealing a homogenous distribution of Si over the entire volume. A significant inhomogeneity, such as nano-precipitates, is not observed. Beside some surface oxidation due to sample preparation, no impurities are detected in Si, neither inside the bulk grain nor at the GB. The same observation was confirmed for another APT analysis performed on the same $\Sigma 3$ (111) from Position ①. If impurities are present in the Si, then their concentrations in the bulk as well as at the GB are below the detection limit of the APT, which is in the range of 10^{18} at/cm³ in our measurements. To be precise, the detection limit for Cu is 2×10^{18} at/cm³ in the small cylinder as shown in

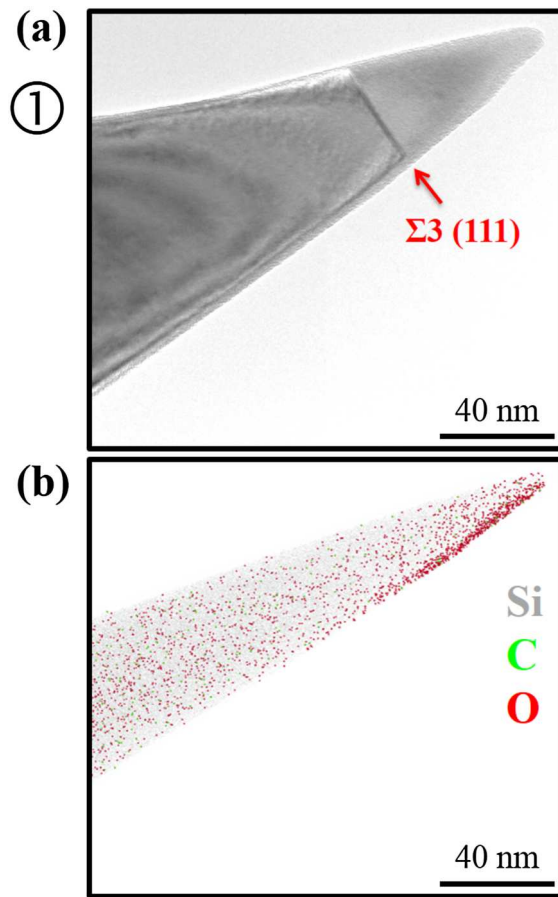


Figure 4. (a) Transmission electron microscopy image of the final atom probe tomography tip taken from $\Sigma 3$ (111) twin boundary at Position ① showing the position of the boundary 67 nm away from the apex of the tip. (b) Correlative three-dimensional elemental map with Si atoms in gray, C in green, and O in red.

Figure 7(a). The absence of impurities at this GB is not surprising, as the analyzed GB is a fully coherent $\Sigma 3$ (111) TB, which has a negligible density of defects, practically no free volume, and hence negligible impurity solubility

[9]. Our APT results obtained on a $\Sigma 3$ (111) TB are in agreement with those published recently by Ohno [25].

Figure 5 shows the 3D elemental map of a small region of interest of the R 55.4° GB taken from region ② and the corresponding one-dimensional concentration profile. C and O decorations of the GB can be clearly seen in the elemental map. The local C and O concentrations are in the range of 0.3 at.%. Although the sample was intentionally contaminated with Fe and Cu, no metal impurities were detected at this specific region of the GB, as can be seen in the mass spectrum of the measured cylinder in Figure 6. We note at this point that APT is sensitive to all possible impurity species, even if they were not expected. Every peak in a spectrum is assigned to a specific complex. All the measurements typically have the main peaks at 14–15 Da, representing double-charged Si isotopes. The APT tip is heated up by the laser during the measurement, leading to thermal tails for Si peaks. The single-charged peaks at 28–30 Da are orders of magnitude smaller with the chosen measurement parameters. H_{1-2}^+ can be found

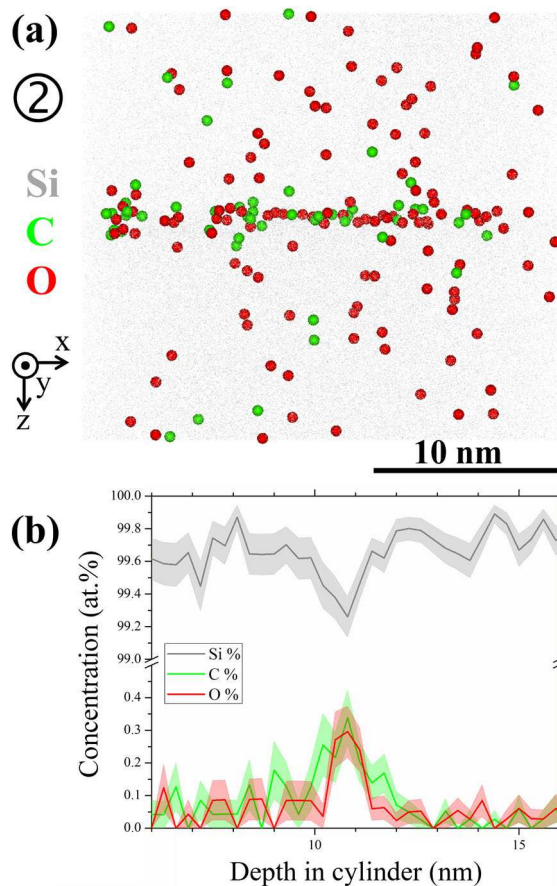


Figure 5. (a) Projection of three-dimensional elemental map of a small cylinder ($R = 13$ nm and $h = 23$ nm) taken from atom probe tomography analysis of the R 55.4° grain boundary at Position ②. C and O atoms are plotted larger for better visualization. (b) Correlative one-dimensional concentration profile along the normal of the grain boundary (0.3 nm sampling box).

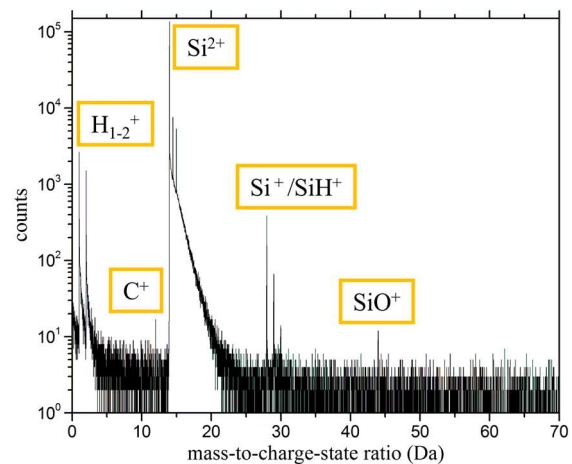


Figure 6. Time-of-flight mass spectrum corresponding to the small volume around the grain boundary shown in Figure 5(a).

in every APT measurement and is due to residual H in the analysis chamber. C appears monoatomic and single charged, whereas O typically is detected as SiO. No peaks outside of the shown segment (0–70 Da) were detected. Concerning Fe, a certain uncertainty lies in the analysis of the corresponding time-of-flight mass spectra. This is caused by the fact that the main isotope of Fe has the atomic mass of 56 Da, while the main isotope of Si has the atomic mass of 28 Da. This coincidence can lead to peak overlap of the Fe^{2+} and Si^{1+} ions in the spectra. A decomposition of the peaks taking the abundance of the different isotopes into account revealed though that the peak at 28 Da most likely pertains to Si^{1+} . Even if the peak was assigned to be Fe^{2+} , no segregation can be observed at the GB position. The absence of transition metal impurities at this GB can be due to either the formation of silicides [48] so that no solute impurities are left to segregate at GBs, or to a very low concentration of the impurities at the GB, falling below the detection limit of APT. Likewise, the concentration of the B dopants lies below the detection limit, and so, no B was detected in any of our measurements. We point out here that in case of segregation, the local concentration of impurities within the small reference volume measured by APT will easily exceed the detection limit.

Figure 7 shows the 3D elemental map and one-dimensional concentration profile for a specific region of the GB shown in Position ③. This GB segment corresponds to R 32.1°. This was double checked by conducting an additional EBSD scan directly on the APT tip during sample preparation. In the APT measurement, we could not detect any enrichment of O at the GB, and the concentration of C is distinctly lower than for the random GB shown in Figure 5, namely, only 0.1 at.%. However, the same data set reveals Cu decoration of the R 32.1° located between two triple points.

To quantify the amount of impurities segregated at the GBs shown in Figures 4, 5, and 7, we extract the Gibbs' interfacial excess Γ from the APT data for the different

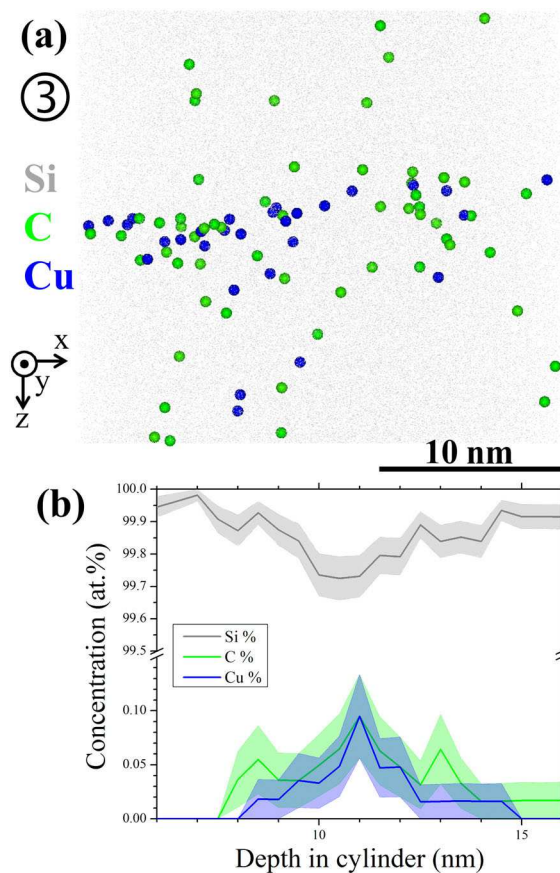


Figure 7. (a) Projection of three-dimensional elemental map of a small cylinder ($R = 13$ nm and $h = 23$ nm) taken from atom probe tomography analysis of the R 32.1° grain boundary at Position ③. C and Cu atoms are plotted larger for better visualization. (b) Correlative one-dimensional concentration profile along the normal of the grain boundary (0.5 nm sampling box).

atomic species by the method presented in [49]. Table I gives an overview of the different measurements including the GB character, excess values, and the corresponding local EBIC contrast values. Measurements at the GB regions ①–③ are marked with the same label in the table. The other measurements were taken from the same ingot but from another area. In some cases, only qualitative EBIC data are available. There was a distinct EBIC contrast observable at these positions, so we just give the estimation $>>1\%$ here.

4. DISCUSSION

The correlative EBSD–EBIC–APT analysis presented here provides detailed information on the GB segregation. First of all, the correlation of the GB crystallography provided by EBSD with the local recombination activity provided by EBIC in principle matches expectations that low indexed coherent TBs exhibit a low recombination activity, whereas random GBs and higher order TBs show a strong

recombination activity. This was already shown before by several authors [17,50]. What was not taken into account in most of the studies though are the GB plane and its influence on the recombination activity. As described before, the GB is described by five parameters, and each of them might influence the electrical properties of the interface. This can explain the observed differences in EBIC contrast in our study, for example, the changing EBIC contrast along the $\Sigma 3$ in Figure 2(a) and (c).

What cannot be deduced from the EBSD–EBIC data is, whether the distorted GB crystallography alone or rather their interaction with impurities and the following impurity segregation leads to the enhanced recombination activity. This can only be answered in correlation with the exact GB chemistry. Former studies postulated the presence of transition metals at these GBs [43,51]. For the first time, we are now able to give quantitative values for the impurity segregation by using APT (Table I). A direct correlation of the GB crystallography with the detected impurity excess is now possible. Indeed, this work gives for the first time direct evidence on the dependence between impurity segregation and GB character. That is to say that the total impurity excess Γ_{total} at the GB is increasing with the GB symmetry: $\Gamma_{\text{total},\Sigma 3} < \Gamma_{\text{total},\Sigma 9} < \Gamma_{\text{total},\Sigma 27} < \Gamma_{\text{total},R}$. Although this trend would be expected, it was never been measured before in a quantitative manner. Surprisingly though, no Fe was detected in any of our measurements, and Cu was only detected in one sample. According to the neutron activation analysis (Figure 1), the total Cu content in the bulk material of the studied sample is expected to be a few 10^{16} at/cm³, whereas the Fe content is smaller by about one order of magnitude. Indeed, if all the dissolved Fe and Cu atoms were distributed homogeneously on interstitial sites in the sample, then it would not be possible to detect their respective low concentrations with the given detection limit of the APT. However, a homogenous distribution of the impurities is very unlikely, as the mc-Si formed during crystallization contains extended defects such as dislocations and GBs as well as point defects. Knowing that the solubility of Fe and Cu is far below the dissolved concentration of these species during cooling of the ingot, they are expected to segregate at defects and might also form precipitates as shown in [27]. With respect to the analyzed GBs, a local enrichment of the Fe and Cu concentration may be expected, especially at the GBs where elevated recombination activity was observed.

The fact that we only observe Cu but no Fe in the APT analysis can have different reasons. (i) Fe is detected only as Fe^{2+} ions in the APT measurements and cannot be separated from the Si^{1+} peak, as already discussed earlier. (ii) The solubility of Fe in Si is much lower than that of Cu and drops steeply upon decrease of temperature (ratio of Cu to Fe solubility about 10^2 at 1100 °C and 10^4 at 700 °C [52]). For example, at 1100 °C, the solubility of Cu in Si is about 5×10^{17} at/cm³, whereas for Fe, it is only 3×10^{15} at/cm³ [7]. This can lead to a preferred precipitation of Fe already at an earlier stage in the cooling process of the ingot. A high amount of Fe precipitates reduces the concentration

of dissolved Fe in the residual material. Accordingly, the concentration can fall easily below the detection limit for the majority of the GBs. (iii) The diffusivity of Cu in Si is much higher than for Fe [7,52]. Even at room temperature, Cu is still mobile and, hence, can easily decorate dislocations and GBs.

Although we do not have the quantitative EBIC data for all the measurements, we see from the data in Table I that impurities are only detected for GBs with a distinct EBIC contrast. Indeed, the three qualitative EBIC measurements showed a strong contrast $\gg 1$. Nevertheless, no direct trend between the EBIC and the APT data is observed, like we showed before between the EBIC and the APT results. This can be explained by several reasons. (i) The EBIC contrast might be influenced by impurity concentration below the detection limit of 10^{18} at/cm³, but it is very unlikely that such small concentrations have a significant influence. (ii) We are analyzing a very small volume by APT and thus only a very small segment of the GB, whereas the EBIC signal is generated from a comparatively large volume. Segregated impurities may not be distributed homogeneously along the GB. This effect can already be seen in our APT measurements at the $\Sigma 9$ GB with a misorientation of 38.4°. Here we have APT datasets of GB segments, where the distance between the single segments was not bigger than 5 μm . The detected carbon excess Γ_c lies between 0.13 at/nm² and 0.23 at/nm². Nevertheless, the impurity decoration of the GBs in the 3D elemental maps within a single dataset appears homogeneously, and a huge inhomogeneity has not been detected so far. (iii) We detect different atomic species segregated at the GBs. Their individual influence on the recombination activity might be profoundly different. The only measurement where we could detect Cu segregation originates from the GB with the highest EBIC contrast. This is in agreement with the literature, where the transition metals are known to influence the electrical properties of Si solar cells a lot [16]. Moreover, the current correlative EBIC–APT study shows that C and O may also contribute to the strong recombination activity observed for some of the GBs in mc-Si solar cells. In more detail, C segregation is found in every single measurement of the recombination active (contrast $>1\%$) GBs. In case of the $\Sigma 9$ interface, C was even the only detected impurity species (Table I). O segregation is found for a $\Sigma 27b$ and the R GB at Position ②. In these two measurements, the O/C ratio is higher for the GB with the stronger EBIC contrast. At this stage, no clear statement can be made though on the difference in the specific influence of these light impurities on the GB recombination. Now, further studies are necessary to understand the mechanism that explains the impact of each kind of impurity on the electrical properties of mc-Si.

Notable at this point is the difference in segregation behavior of the R GBs at Positions ② and ③: C and O segregation is found at Position ②, whereas C and Cu segregation is found at Position ③. First of all, we need to be aware of the small volume analyzed by APT; the impurity concentrations might vary in the surrounding GB

volume. Therefore, it is hard to extract general statements from these data. Beside this, there are different possible reasons for this observation: (i) both GBs differ extremely in length. Position ② refers to a GB, which is several hundred micrometers long, while the one at Position ③ has a length of only ~ 10 μm . This could indicate a stronger distortion of the atomic arrangements at Position ③, which might influence the interaction with impurities. (ii) The different impurity species might mutually influence their segregation behavior. Segregation of Cu might prevent the segregation of O for example. (iii) Position ③ lies in close vicinity of two triple junctions. These triple junctions can strongly influence the diffusivity of impurities; hence, they can also affect segregation.

In case of dislocations, Kveder *et al.* [3] assigned the enhanced recombination activity to a contamination by transition metals. In particular, at room temperature, dislocations were only visible by EBIC if they were contaminated. We find a similar behavior for the GBs analyzed by APT; only the GBs with significant recombination activity at room temperature show a detectable impurity

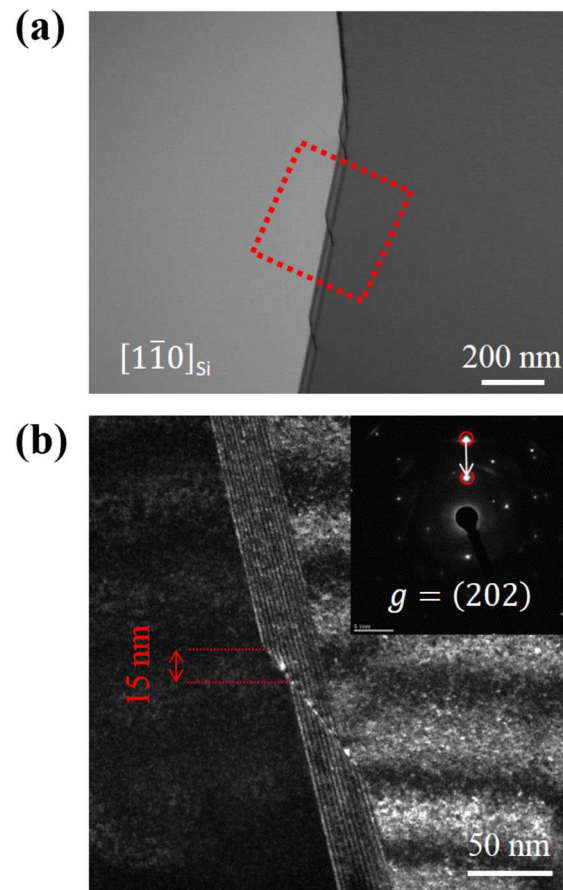


Figure 8. (a) Scanning transmission electron microscopy bright field image of a curved R 39.5° grain boundary showing several dislocations. (b) Weak-beam dark-field image of the same grain boundary with step appearing bright in two beam conditions $g = (202)$.

decoration, although the impurities are not limited to transition metals in our case. These decorated GBs do not show a perfect symmetry as explained earlier. Indeed, for random GBs and incoherent TBs, a high defect density and thus enhancement in the impurity segregation is expected. For example, the curvature of a GB can be composed by several steps accompanied very often by dislocations as shown by Wang *et al.* [53]. In addition, TEM investigations were performed on another region of the same sample; we also observed huge steps with a length of ≈ 15 nm on a random GB with a misorientation of 39.5° and with an EBIC contrast of 14% (Figure 8). The same mechanism holds for the TBs, where a deviation in misorientation or boundary plane position is accommodated by defects, which again enhance the interaction with impurities. In this way, we conclude in this section that the recombination activity observed for the incoherent TBs and random GBs in Figure 2 is mainly due to defects accumulated at the boundary plane leading to accommodation of the impurities. These findings are in agreement with the existing studies in the literature, where contamination and CSL character of the GBs were found to have an influence on the electrical properties of GBs [17,54].

5. CONCLUSIONS

For the first time, we were able to show the presence of different impurity species decorating GBs in mc-Si with atomic-scale resolution in a quantitative manner. The correlated EBSD–EBIC–APT studies suggest that the segregation of impurities is strongly affected by the GB properties, in particular its coherency. Highly symmetric TBs show nearly no interaction with impurities, in contrast to high-angle random GBs and higher order TBs or incoherent portions of TBs. Thus, we conclude that only by taking the full GB characteristics into account and correlating it with the local chemistry, a deeper understanding of GB recombination can be achieved. The statement of a specific CSL value alone is not sufficient to characterize the recombination activity of GBs. This is especially important for the further development of mc-Si for solar cells with high efficiencies.

In agreement with the literature, we find that Cu impurities have a strong impact on the recombination activity. Because of its low concentration and peak overlap in the mass spectrum, it is not possible to give a clear statement on the role of Fe on GB recombination at this stage. Furthermore, the present EBSD–EBIC–APT studies suggest that besides the transition metals C and O may also play an important role for the recombination activity of the GBs in mc-Si solar cells.

ACKNOWLEDGEMENTS

The authors would like to thank Dr. Otwin Breitenstein for the fruitful discussions about the interpretation of

the EBIC data and Dr. Aleksander Kostka for the professional support in HRTEM analysis. This work was funded by the Federal Ministry of Education and Research (BMBF 03X5522). It was also partially supported by the Federal Ministry for the Environment (BMU) under contract number 0325270D.

REFERENCES

1. Di Sabatino M, Stokkan G. Defect generation, advanced crystallization, and characterization methods for high-quality solar-cell silicon. *Physica Status Solidi A* 2013; **210**: 641–648.
2. Proceedings of 6th world conference on photovoltaic energy conversion, 2014 in print.
3. Kveder V, Kittler M, Schröter W. Recombination activity of contaminated dislocations in silicon: a model describing electron-beam-induced current contrast behavior. *Physical Review B* 2001; **63**: 115208.
4. Yang YM, Yu A, Hsu B, Hsu WC, Yang A, Lan CW. Development of high-performance multicrystalline silicon for photovoltaic industry. *Progress in Photovoltaics: Research and Applications* 2015; **23**: 340–351.
5. Lejček P. *Grain Boundary Segregation in Metals*. Springer-Verlag: Berlin, 2010.
6. Sutton AP, Balluffi RW. *Interfaces in Crystalline Materials*. Clarendon Press; Oxford University Press: Oxford, New York, 1995.
7. Peaker AR, Markevich VP, Hamilton B, Parada G, Dudas A, Pap A, Don E, Lim B, Schmidt J, Yu L, Yoon Y, Rozgonyi G. Recombination via point defects and their complexes in solar silicon. *Physica Status Solidi A* 2012; **209**: 1884–1893.
8. Gao B, Nakano S, Kakimoto K. Reduction of oxygen impurity in multicrystalline silicon production. *International Journal of Photoenergy* 2013; **2013**: 1–6.
9. Nakajima K, Usami N. *Crystal Growth of Si for Solar Cells*. Springer Verlag: Berlin, 2009.
10. Pizzini S, Cagnoni P, Sandrinelli A, Anderle M, Canteri R. Grain boundary segregation of oxygen and carbon in polycrystalline silicon. *Applied Physics Letters* 1987; **51**: 676.
11. Pizzini S, Sandrinelli A, Beghi M, Narducci D, Allegretti F, Torchio S, Fabbri G, Ottaviani GP, Demartin F, Fusi A. Influence of extended defects and native impurities on the electrical-properties of directionally solidified polycrystalline silicon. *Journal of the Electrochemical Society* 1988; **135**: 155–165.
12. Istratov AA, Buonassisi T, Pickett MD, Heuer M, Weber ER. Control of metal impurities in “dirty” multicrystalline silicon for solar cells. *Materials Science and Engineering B* 2006; **134**: 282–286.

13. Buonassisi T, Istratov AA, Pickett MD, Heuer M, Kalejs JP, Hahn G, Marcus MA, Lai B, Cai Z, Heald SM, Ciszek TF, Clark RF, Cunningham DW, Gabor AM, Jonczyk R, Narayanan S, Sauar E, Weber ER. Chemical natures and distributions of metal impurities in multicrystalline silicon materials. *Progress in Photovoltaics: Research and Applications* 2006; **14**: 513–531.
14. Istratov AA, Buonassisi T, McDonald RJ, Smith AR, Schindler R, Rand JA, Kalejs JP, Weber ER. Metal content of multicrystalline silicon for solar cells and its impact on minority carrier diffusion length. *Journal of Applied Physics* 2003; **94**: 6552–6559.
15. Davis JR, Rohatgi A, Hopkins RH, Blais PD, Raichoudhury P, McCormick JR, Mollenkopf HC. Impurities in silicon solar-cells. *IEEE Transactions on Electron Devices* 1980; **27**: 677–687.
16. Coletti G, Bronsveld PCP, Hahn G, Warta W, Macdonald D, Ceccaroli B, Wambach K, Le Quang N, Fernandez JM. Impact of metal contamination in silicon solar cells. *Advanced Functional Materials* 2011; **21**: 879–890.
17. Chen J, Sekiguchi T, Yang D, Yin F, Kido K, Tsunekawa S. Electron-beam-induced current study of grain boundaries in multicrystalline silicon. *Journal of Applied Physics* 2004; **96**: 5490.
18. Chen J, Sekiguchi T, Ito S, Yang DR. Carrier recombination activities and structural properties of small-angle boundaries in multicrystalline silicon. *Solid State Phenomena* 2008; **131–133**: 9–14.
19. Zuschlag A, Micard G, Junge J, Kas M, Seren S, Hahn G, Coletti G, Jia G, Seifert W. Investigations on the recombination activity of grain boundaries in MC silicon. In *Photovoltaic Specialists Conference, 2008. PVSC'08. 33rd IEEE* 2008; 1–5.
20. Lausch D, Petter K, Bakowskie R, Bauer J, Breitenstein O, Hagendorf C. Classification and investigation of recombination-active defect structures in multicrystalline silicon solar cells. Proceedings of the 27th EUPVSEC, 2012; 723–728.
21. Hähnel A, Bauer J, Blumtritt H, Breitenstein O, Lausch D, Kwapil W. Electron microscope verification of prebreakdown-inducing α -FeSi₂ needles in multicrystalline silicon solar cells. *Journal of Applied Physics* 2013; **113**: 044505.
22. Jiang T, Yu X, Gu X, Rozgonyi G, Yang D. Modulation of electrical characteristics at a Ni-contaminated silicon grain boundary by engineering the metal precipitates. *Physica Status Solidi A* 2013; **210**: 1828–1831.
23. Stoffers A, Cojocaru-Miredin O, Breitenstein O, Seifert W, Zaefferer S, Raabe D. Grain boundary characterization in multicrystalline silicon using joint EBSD, EBIC, and atom probe tomography. Photovoltaic specialist conference (PVSC), 2014 IEEE 40th: IEEE, 2014; p. 0042–6.
24. Herbig M, Choi P, Raabe D. Combining structural and chemical information at the nanometer scale by correlative transmission electron microscopy and atom probe tomography. *Ultramicroscopy* 2015; **153**: 32–39.
25. Ohno Y, Inoue K, Tokumoto Y, Kutsukake K, Yonenaga I, Ebisawa N, Takamizawa H, Shimizu Y, Inoue K, Nagai Y, Yoshida H, Takeda S. Three-dimensional evaluation of gettering ability of Sigma 3{111} grain boundaries in silicon by atom probe tomography combined with transmission electron microscopy. *Applied Physics Letters* 2013; **103**: 102102.
26. Gorman BP, Guthrey HL, Al-Jassim MM. Quantification of atomic scale defects in poly Si PV devices using atom probe tomography. 2012 38th IEEE photovoltaic specialists conference (PVSC), 2012; 1498–1500.
27. Riepe S, Reis IE, Kwapil W, Falkenberg MA, Schön J, Behnken H, Bauer J, Kreßner-Kiel D, Seifert W, Koch W. Research on efficiency limiting defects and defect engineering in silicon solar cells—results of the German research cluster SolarFocus. *Physica Status Solidi C* 2011; **8**: 733–738.
28. Reis IE, Riepe S, Koch W, Bauer J, Beljakowa S, Breitenstein O, Habenicht H, Kreßner-Kiel D, Pensl G, Schön J, Seifert W. Effect of impurities on solar cell parameters in intentionally contaminated multicrystalline silicon. Proceedings 24th European photovoltaic solar energy conference, Hamburg, Germany, 2009; 2144–2148.
29. Kelly TF, Larson DJ. Atom probe tomography 2012. *Annual Review of Materials Research* 2012; **42**: 1–31.
30. Gault B, Moody MP, Cairney JM, Ringer SP. *Atom Probe Microscopy*. Springer Science+Business Media: New York, NY, USA, 2012.
31. Duarte MJ, Klemm J, Klemm SO, Mayrhofer KJJ, Stratmann M, Borodin S, Romero AH, Madinehei M, Crespo D, Serrano J, Gerstl SSA, Choi PP, Raabe D, Renner FU. Element-resolved corrosion analysis of stainless-type glass-forming steels. *Science* 2013; **341**: 372–376.
32. Cojocaru-Miredin O, Choi P, Wuerz R, Raabe D. Exploring the p-n junction region in Cu(In,Ga)Se-2 thin-film solar cells at the nanometer-scale. *Applied Physics Letters* 2012; **101**: 181603.
33. Keller J, Schlesiger R, Riedel I, Parisi J, Schmitz G, Avellan A, Dalibor T. Grain boundary investigations on sulfurized Cu(In,Ga)(S,Se)(2) solar cells using atom probe tomography. *Solar Energy Materials and Solar Cells* 2013; **117**: 592–598.

34. Cadel E, Barreau N, Kessler J, Pareige P. Atom probe study of sodium distribution in polycrystalline Cu(In, Ga)Se-2 thin film. *Acta Materialia* 2010; **58**: 2634–2637.
35. Felfer PJ, Alam T, Ringer SP, Cairney JM. A reproducible method for damage-free site-specific preparation of atom probe tips from interfaces. *Microscopy Research and Technique* 2012; **75**: 484–491.
36. Priester L. *Grain Boundaries from Theory to Engineering*. Springer Series in Materials Science 172. Springer: Dordrecht, 2013.
37. Ganapati V, Schoenfelder S, Castellanos S, Oener S, Koepge R, Sampson A, Marcus MA, Lai B, Morhenn H, Hahn G, Bagdahn J, Buonassisi T. Infrared birefringence imaging of residual stress and bulk defects in multicrystalline silicon. *Journal of Applied Physics* 2010; **108**: 063528.
38. Sarau G, Christiansen S, Holla M, Seifert W. Correlating internal stresses, electrical activity and defect structure on the micrometer scale in EFG silicon ribbons. *Solar Energy Materials and Solar Cells* 2011; **95**: 2264–2271.
39. Brandon DG. Structure of high-angle grain boundaries. *Acta Metallurgica et Materialia* 1966; **14**: 1479–1484.
40. Ram F, Zaefferer S, Raabe D. Kikuchi bandlet method for the accurate deconvolution and localization of Kikuchi bands in Kikuchi diffraction patterns. *Journal of Applied Crystallography* 2014; **47**: 264–275.
41. Wolf U, Ernst F, Muschik T, Finnis MW, Fischmeister HF. The influence of grain-boundary inclination on the structure and energy of sigma=3 grain-boundaries in copper. *Philosophical Magazine A* 1992; **66**: 991–1016.
42. Miyazawa K, Iwasaki Y, Ito K, Ishida Y. Combination rule of Sigma values at triple junctions in cubic polycrystals. *Acta Crystallographica. Section A* 1996; **52**: 787–796.
43. Chen B, Chen J, Sekiguchi T, Saito M, Kimoto K. Structural characterization and iron detection at Sigma 3 grain boundaries in multicrystalline silicon. *Journal of Applied Physics* 2009; **105**: 113502.
44. Randle V. Twinning-related grain boundary engineering. *Acta Materialia* 2004; **52**: 4067–4081.
45. Shariq A, Mutas S, Wedderhoff K, Klein C, Hortenbach H, Teichert S, Kucher P, Gerstl SS. Investigations of field-evaporated end forms in voltage- and laser-pulsed atom probe tomography. *Ultramicroscopy* 2009; **109**: 472–479.
46. Vurpillot F, Gruber M, Da Costa G, Martin I, Renaud L, Bostel A. Pragmatic reconstruction methods in atom probe tomography. *Ultramicroscopy* 2011; **111**: 1286–1294.
47. Cojocaru-Miredin O, Schwarz T, Choi P, Herbig M, Wuerz R, Raabe D. Atom probe tomography studies on the Cu(In,Ga)Se₂ grain boundaries. *Journal of Visualized Experiments* 2013; (74): 1–8.
48. Schon J, Haarahiltunen A, Savin H, Fenning DP, Buonassisi T, Warta W, Schubert MC. Analyses of the evolution of iron-silicide precipitates in multicrystalline silicon during solar cell processing. *IEEE Journal of Photovoltaics* 2013; **3**: 131–137.
49. Krakauer BW, Seidman DN. Absolute atomic-scale measurements of the Gibbsian interfacial excess of solute at internal interfaces. *Physical Review B* 1993; **48**: 6724–6727.
50. Kojima T, Tachibana T, Kojima N, Ohshita Y, Arafune K, Ogura A, Yamaguchi M. Nickel distribution and recombination activity in as-grown and annealed multicrystalline silicon. *Japanese Journal of Applied Physics* 2014; **53**: 04ER20.
51. Chen J, Yang D, Xi Z, Sekiguchi T. Recombination activity of Σ3 boundaries in boron-doped multicrystalline silicon: influence of iron contamination. *Journal of Applied Physics* 2005; **97**: 033701.
52. Weber ER. Transition-metals in silicon. *Applied Physics A-Materials Science and Processing* 1983; **30**: 1–22.
53. Wang HY, Usami N, Fujiwara K, Kutsukake K, Nakajima K. Microstructures of Si multicrystals and their impact on minority carrier diffusion length. *Acta Materialia* 2009; **57**: 3268–3276.
54. Buonassisi T, Istratov AA, Pickett MD, Marcus MA, Ciszek TF, Weber ER. Metal precipitation at grain boundaries in silicon: dependence on grain boundary character and dislocation decoration. *Applied Physics Letters* 2006; **89**: 042102.